*International Journal of Minerals, Metallurgy and Materials*
*Volume 25, Number 11, November 2018, Page 1294*
**https://doi.org/10.1007/s12613-018-1682-8**

# Microstructural evolution and mechanical properties of friction stir-welded C71000 copper–nickel alloy and 304 austenitic stainless steel

*Hamed Jamshidi Aval*

Department of Materials and Industrial Engineering, Babol Noshirvani University of Technology, Shariati Avenue, Babol, 47148-71167, Iran

(Received: 20 February 2018; revised: 29 May 2018; accepted: 11 June 2018)

**Abstract:** Dissimilar joints comprised of copper–nickel and steel alloys are a challenge for manufacturers in modern industries, as these metals are not thermomechanically or chemically well matched. The present study investigated the effects of tool rotational speed and linear speed on the microstructure and mechanical properties of friction stir-welded C71000 copper–nickel and 340 stainless steel alloys using a tungsten carbide tool with a cylindrical pin. The results indicated that a rotational-to-linear speed ratio of 12.5 r/mm did not cause any macro defects, whereas some tunneling defects and longitudinal cracks were found at other ratios that were lower and higher. Furthermore, chromium carbide was formed on the grain boundaries of the 304 stainless steel near the shoulder zone and inside the joint zone, directing carbon and chromium penetration toward the grain boundaries. Tensile strength and elongation percentages were 84% and 65% of the corresponding values in the copper–nickel base metal, respectively.

**Keywords:** dissimilar friction stir welding; copper–nickel alloy; austenitic stainless steel; microstructure; mechanical properties

## 1. Introduction

Copper–nickel alloys exhibit substantial corrosion resistance and anti-algae properties against biological sediments. Pure copper is not stable in oxygenated electrolytes, especially in marine and chlorine ion environments where copper–nickel alloys are widely used, with copper as the main component [1]. The addition of nickel to copper improves the mechanical strength, durability, and resistance to corrosion, abrasion, and cavitation in sea and polluted water. This alloy also exhibits significant stress corrosion cracking and corrosion fatigue resistance. Corrosion resistance can be increased by adding more nickel to copper–nickel alloys [2]. Since these alloys can be easily assembled and welded, they are prime candidates for plumbing systems, ship bodies, and other marine structures.

Generally, stainless steel plays a major role in the modern world. Welding of austenite stainless steel is known for two important properties: maintenance of corrosion resistance and prevention of crack formation. Dissimilar joints of coatings on offshore platform insulators, achieved by different techniques, are among copper–nickel plate applications for corrosion prevention. Other applications include the joining of copper–nickel pipes with steel flanges and/or direct joining of these pipes with steel pipes in marine industries [3].

Nevertheless, welding of dissimilar metals is always challenging because of numerous factors. These include different melting points, thermal conductivity, and thermal expansion coefficients; galvanic corrosion; the high solidification rate of molten copper; entry of molten copper into steel grain boundaries (especially in the heat-affected zone (HAZ)); formation of hot cracks; high copper oxidation at high temperatures; and type of filler metal [4–9]. It is essential to select the appropriate filler metal and welding parameters for dissimilar-metal fusion welding of copper–nickel and stainless steel alloys in order to reduce probable defects (e.g., cavitation and gas cavities).

Recent developments in solid-state welding have made it an alternative to fusion welding. In comparison to other welding techniques, friction-stir welding is a solid-state technique with an outstanding combination of high speed, precision, and variety. Among different welding methods, friction-stir welding of dissimilar alloys is important due to the ability to join alloys with different properties. In addition,

Corresponding author: Hamed Jamshidi Aval E-mail: h.jamshidi@nit.ac.ir

different welding configurations in this method (e.g., lap and butt joints) make it applicable in different situations.

Few studies have been conducted on friction-stir welding of dissimilar copper and stainless steel alloys. In this regard, Imani *et al.* [10] investigated a pure copper and stainless steel joint with a thickness of 3 mm using friction-stir welding. It was found that the tool offset toward the copper side played a significant role in eliminating defects in the joints. In addition, Ramirez *et al.* [11] examined the effects of tool offset on the microstructure and mechanical properties of joints in friction-stir welding of pure copper and 316 stainless steel with a thickness of 2 mm. They studied 0, 0.6, and 1.6 mm offsets relative to the joint interface. When a major part of the tool was on the steel side, the joint efficiency was 55% of copper base metal. Maximum joint efficiency, i.e., 87% of copper base metal, was reported in the 0.6-mm offset relative to the joint interface.

Furthermore, Najafkhani *et al.* [12] studied the joint of pure copper and 316 stainless steel with a thickness of 5 mm using friction-stir welding. In their study, all joints cracked from the heat-affected zone of the copper base metal. The highest tensile strength and elongation percentage were 220 MPa and 7%, respectively. In addition, Shamsujjoha *et al*. [13] studied the lap joint of pure copper with 1018 carbon steel using friction-stir welding. They found that the joining process at the interface was both mechanical and metallurgical. Jafari *et al.* [14] also studied the friction-stir welding of pure copper and 304 stainless steel with a thickness of 3 mm. The heat input from the welding increased the grain size in the heat-affected zone and decreased joint ductility by increasing the number of welding passes.

According to the literature, there are no studies on the friction-stir welding of copper–nickel and austenite stainless steel alloys. Accordingly, the present study investigated the effects of process parameters on the microstructure and mechanical properties of friction stir-welded C71000 copper–nickel and 304 stainless steel alloys using a tungsten carbide tool with a cylindrical pin. Optical microscopy and scanning electron microscopy (SEM) were used to study the microstructure and detect the created phases in different zones. The mechanical properties of joints were also evaluated by tensile and microhardness tests.

## 2. Experimental

In the present study, C71000 copper–nickel and 304 austenite stainless steel plates with thicknesses of 2 mm were used. Both plates were cut perpendicular to the rolled metal direction and had a dimension of 50 mm × 100 mm. The chemical compositions and mechanical properties of alloys are listed in Tables 1 and 2. The plates were welded in a butt joint configuration. The copper–nickel alloy was on the retreating side, while the stainless steel alloy was on the advancing side. According to the literatures [10–11], 0.75 mm of the tool axis was offset to the copper–nickel alloy relative to the joint interface. Fig. 1 shows the schematic of the tool offsetting procedure. A tungsten carbide tool with a cylindrical pin with a height of 1.8 mm was used for welding. Fig. 2 demonstrates the dimensions and geometry of the applied tool in welding and Table 3 indicates the welding parameters. The present study selected two rotational speeds of 800 and 1000 r/min and three linear speeds of 40, 60, and 80 mm/min.

**Table 1. Chemical composition of alloy** wt%

| Alloy | Ni | C | Cu | Cr | Fe | Mn | Zn |
|---|---|---|---|---|---|---|---|
| C71000 | 19.12 | 0.05 | Base | — | 0.05 | 0.01 | 0.9 |
| SS304 | 8.10 | 0.05 | 0.44 | 18.50 | Base | 1.20 | — |

**Table 2. Mechanical properties of alloys**

| Alloy | Ultimate tensile strength / MPa | Yield strength / MPa | Micro-hardness, $HV_{0.1}$ | Elongation / % |
|---|---|---|---|---|
| C71000 | 338 | 110 | 90 | 32 |
| SS304 | 585 | 210 | 152 | 42 |

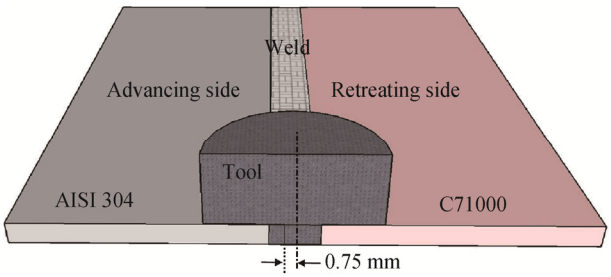


**Fig. 1. Schematic illustration of friction stir butt welding.**

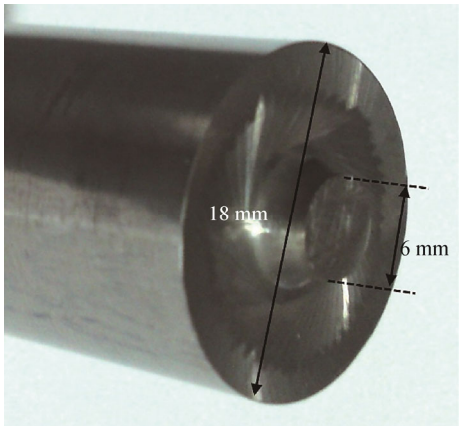


**Fig. 2. Tool geometrical characteristics.**

**Table 3. Friction stir welding process parameters**

| Sample No. | Rotational speed / (r·min$^{-1}$) | Linear speed / (mm·min$^{-1}$) | Rotational-to-linear speed ratio / (r·mm$^{-1}$) |
|---|---|---|---|
| 1 | 800 | 40 | 20.00 |
| 2 | 800 | 60 | 13.33 |
| 3 | 800 | 80 | 10.00 |
| 4 | 1000 | 40 | 25.00 |
| 5 | 1000 | 60 | 16.65 |
| 6 | 1000 | 80 | 12.50 |

The samples were transversely cut for metallographic studies. A marble solution was used for etching the microstructure on the stainless steel side after sanding and polishing, whereas a nitric acid and distilled water solution was used for the copper–nickel alloy. Scanning electron microscopy (SEM) and X-ray diffraction (XRD) were used to evaluate the joint interface and examine the distribution and type of intermetallic compounds in the joint cross section. The mechanical properties of the joint were investigated using a tensile test according to the ASTM E8-M03 standard. The tensile test was carried out at a crosshead speed of 1 mm/min. A Vickers microhardness testing machine with a load of 3 N and test time of 15 s was used to evaluate the hardness distribution of a joint cross section.

## 3. Results and discussion

### 3.1. Weld appearance

The qualitative test of the welded samples indicated that samples No. 1–5 had defects. Longitudinal cracks on the copper–nickel side or tunneling defects on the stainless steel side were observed in all defected samples. Fig. 3 shows the effects of rotational and linear speed on the appearance of welding samples No. 1, 3, 4, and 6, as representative samples containing cracks, tunneling defects, and defect-free welds. It is generally difficult to explain the causes of defects in the samples; however, the heat input may be an influential factor. Many researchers have introduced various analytical, numerical, and empirical models in order to evaluate the relationship between rotational and linear tool speed and heat input and to examine their effects on the temperature distribution in the friction-stir welding procedure. With a proper estimation, the rotational-to-linear speed ratio can be considered a measure of welding heat input.

In this study, samples No. 3 and 4 received the least and most heat input, respectively. The lower temperature of sample No. 3 caused insufficient material flow into the stir zone. After the tool was moved forward, the flow of material stopped before arriving at the advancing side. Therefore, there was inadequate material to fill the hole on the advancing side (stainless steel). The tunnel hole led to the loss of joint strength in this sample, and the two parts were easily separated.

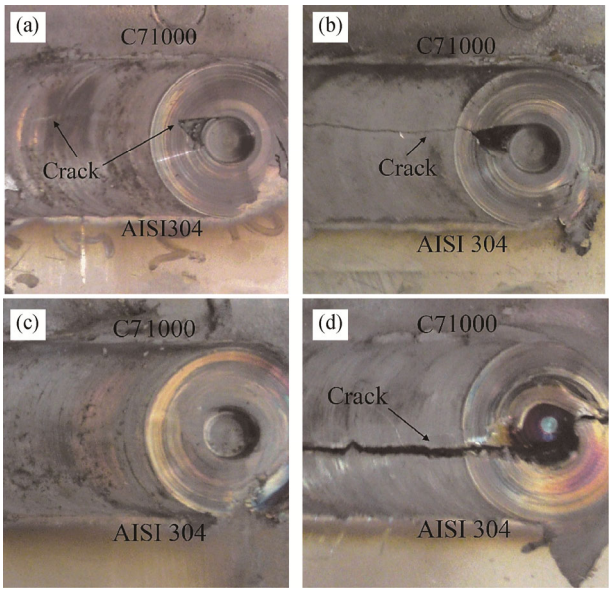


**Fig. 3. Surface appearance of welded samples: (a) No. 4; (b) No. 1; (c) No. 6: (d) No. 3.**

Fig. 3 presents the longitudinal cracks because of a tunneling defect in sample No. 3. Fig. 4 shows the effect of welding heat input on longitudinal crack length. It can be seen that by increasing the rotational-to-linear speed ratio (increasing welding heat input), the maximum temperature in the joint increased, which led to the higher temperature gradient in the welded samples. The significant difference in thermal conductivity of copper–nickel and stainless steel alloys (thermal conductivity of copper–nickel is 2.8 times higher than that of stainless steel) [15–16] at a high temperature gradient produced longitudinal cracks as a result of thermal stress in the joint. According to the visual inspection of welded samples, a tunneling defect developed in the joint at a rotational-to-linear speed ratio of less than 10.00 r/mm.

On the other hand, at the rotational-to-linear speed ratio of 13.33 r/mm or higher, longitudinal cracks were formed at the joint interface.

### 3.2. Macrostructure and microstructure

The evaluation of mechanical and metallurgical properties was only carried out for sample No. 6 because it had no defects. The macrostructure of the joint and microstructure of different zones are shown in Figs. 5 and 6. The microstructure of stainless steel included austenite and δ-ferrite with a grain size of (40 ± 5) μm (Fig. 5(b)). Although the quantity of ferrite phase was not significant, the presence of δ-ferrite could improve the formation of the sigma phase in alloys during friction-stir welding [17].

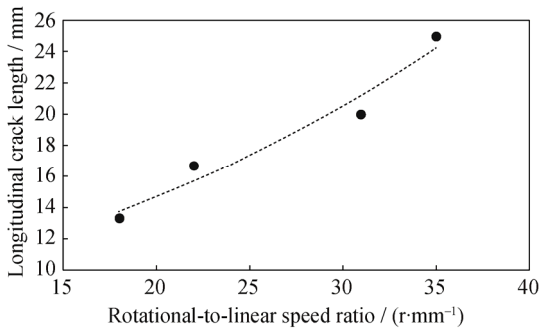


**Fig. 4. Effect of the rotational-to-linear speed ratio on crack length.**

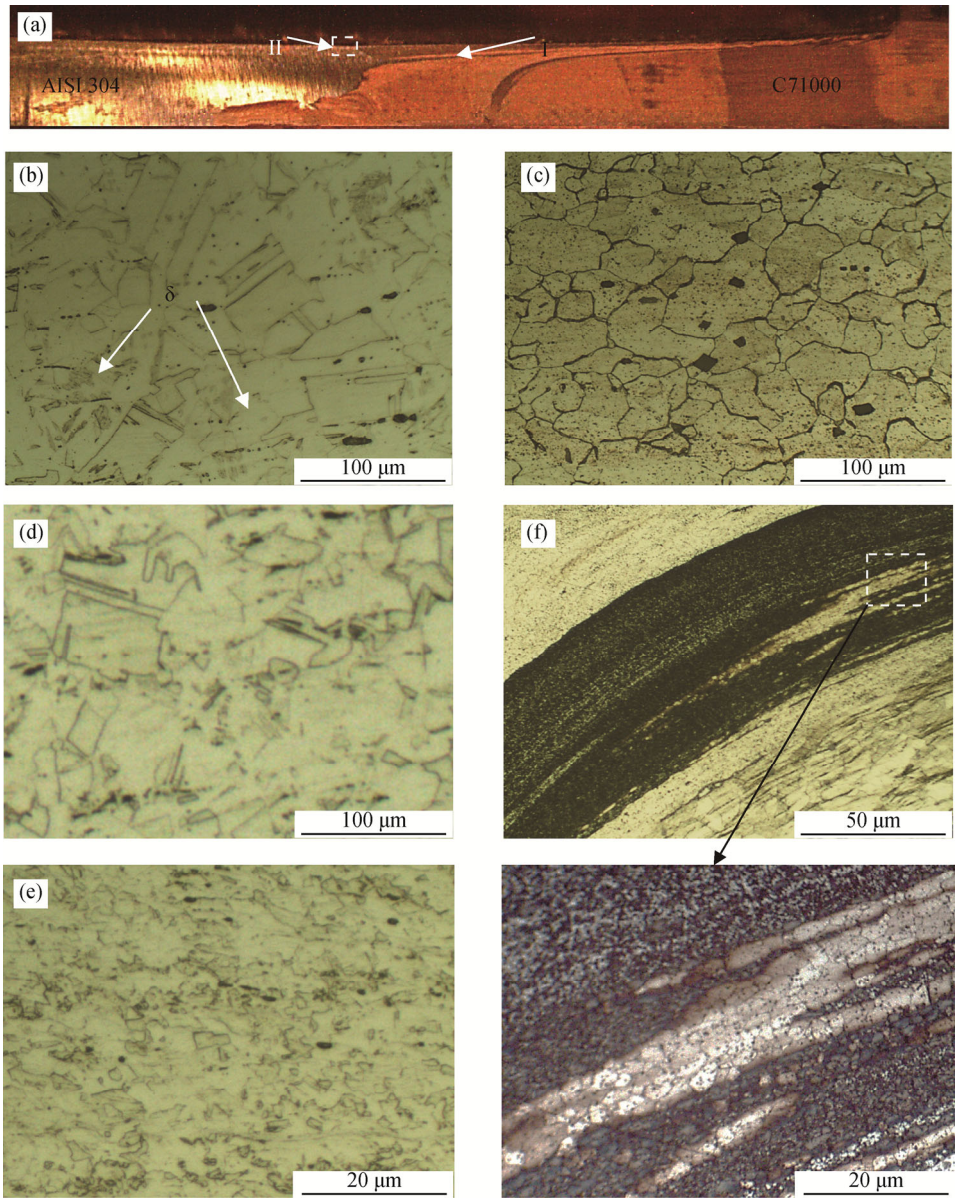


**Fig. 5. Optical images of different zones of sample No. 4: (a) macrostructure of welded sample No. 4; (b) base metal of AISI 304; (c) base metal of C71000; (d) TMAZ in AISI 304 side; (e) SZ in AISI304 side; (f) TMAZ in C71000 side as marked by zone I in (a).**

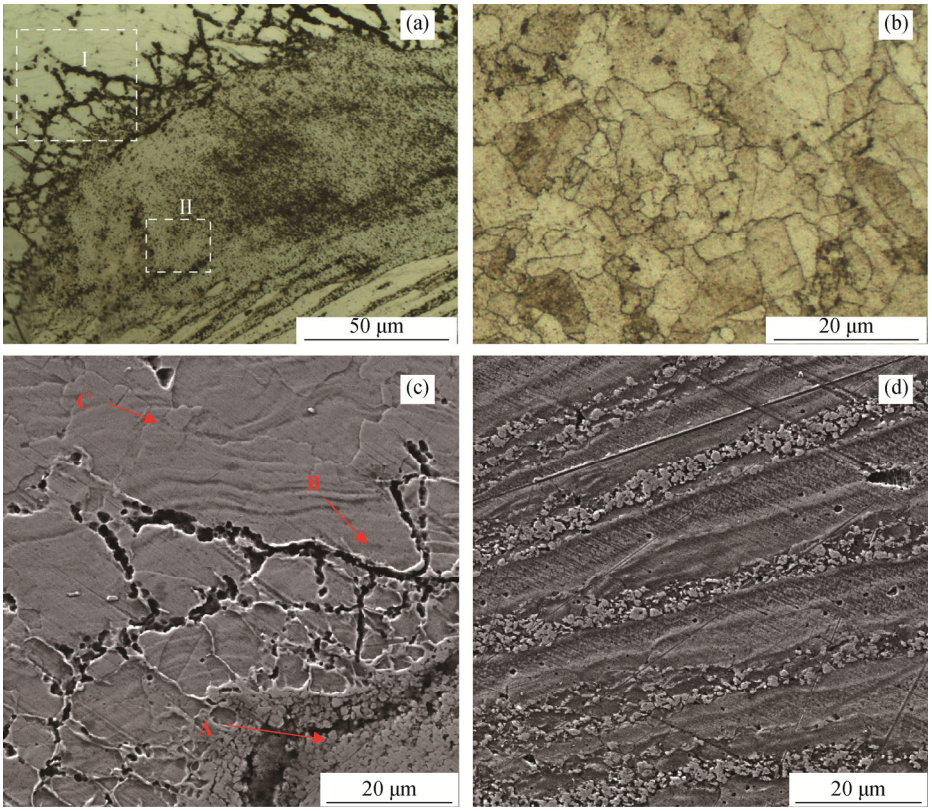


**Fig. 6. Microstructure of stir zone of sample No. 4: (a) microstructure of zone II in Fig. 5(a); (b) SZ in C71000 side; (c) SEM image of zone I in (a); (d) SEM image of zone II in (a).**

The copper–nickel microstructure had a grain size of (50 ± 4) μm and an average particle size of (10 ± 3) μm in the grain boundaries. The results of energy dispersive X-ray spectroscopy (EDS) indicated that these particles were nickel-rich oxides with iron and zinc (Fig. 7). The stir zone mostly consisted of copper–nickel alloy, which was likely due to the lower flow stress of copper–nickel alloy [18] and location of the main part of the tool on the copper–nickel side. Different behaviors of the two alloys in the etchant solution confirmed this finding.

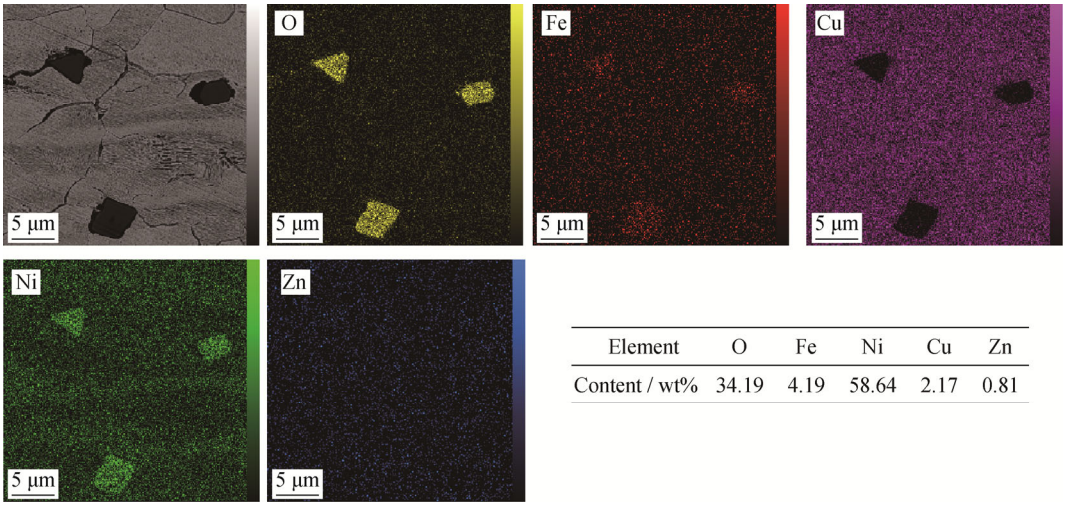


| Element | O | Fe | Ni | Cu | Zn |
|---|---|---|---|---|---|
| Content / wt% | 34.19 | 4.19 | 58.64 | 2.17 | 0.81 |

**Fig. 7. Element mapping result of base metal C71000 alloy.**

As shown in Fig. 5(a), a steel layer was drawn from the advancing zone to the retreating zone (zone I). The joint cross section as a result of friction-stir procedure consisted of the stir zone (SZ), thermomechanically affected zone

(TMAZ), and heat-affected zone (HAZ). The mechanical behaviors of the welding materials, especially the welding zone hardness, were affected by high plastic deformation and high temperature during the friction-stir welding. The stir zone microstructure in the friction-stir weld had smaller and equiaxed grains in comparison with the base metal due to high plastic deformation and stir resulting from the tool pin.

As presented in Fig. 5(f), grains in the thermomechanically affected zone on the copper–nickel side were elongated, which is exclusive to this zone [19]. The steel layer on the copper–nickel side contained recrystallized copper–nickel grains (Fig. 5(f)). On the other hand, the stir zone microstructure on the copper–nickel side contained equiaxed grains with a size of (15 ± 4) μm as a result of dynamic recrystallization in this zone (Fig. 6(b)). The oxide particles observed in the copper–nickel base metal are shown in this figure. These particles were mainly at grain boundaries with a size of (5 ± 2) μm and prevented the growth of stir-zone grains.

The EDS results showed that zinc and iron concentrations in the oxide particles increased (Figs. 7 and 8). The stir zone on the steel alloy side contained small recrystallized grains with a size of (5 ± 1) μm (Fig. 5(e)). Clearly, the grain size in the copper–nickel stir zone was greater than that of the steel-stir zone. The temperature and deformation rate in the friction-stir procedure had inverse effects on the grain size of the stir zone. In fact, an increase in the deformation rate led to a reduced grain size, and a rise in temperature increased the grain size in the stir zone [20].

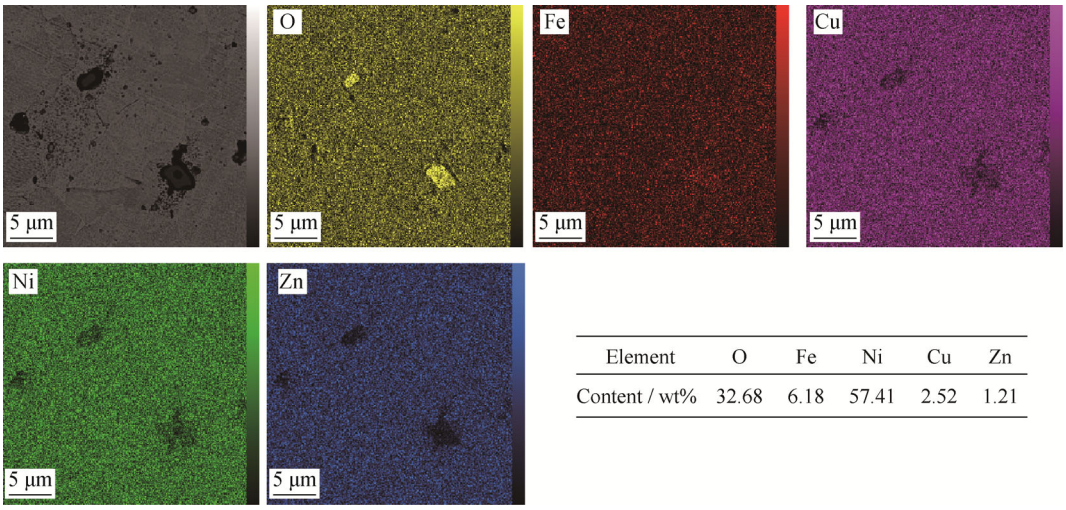


| Element | O | Fe | Ni | Cu | Zn |
|---|---|---|---|---|---|
| Content / wt% | 32.68 | 6.18 | 57.41 | 2.52 | 1.21 |

**Fig. 8. Element mapping result of stir zone of C71000 side.**

The advancing side showed the highest temperature and deformation [21]. According to the stir zone microstructure results, the deformation effect was dominant on the steel side, and the grain size of stir zone reduced relative to the copper–nickel alloy side. On the contrary, elongated grains did not exist in the thermomechanically affected zone on the steel side (Fig. 5(d)). However, annealing twins were found across the base metal, whereas there were fewer twins in the thermomechanically affected zone of the steel. There were no twins in the stir zone on the steel side. An interesting point in the microstructure study was the occurrence of a specific layer-by-layer structure at the interface between copper–nickel and steel alloys near the tool shoulder (Fig. 6(a)). The SEM images of different zones in Fig. 6(a) are presented in Figs. 6(c) and 6(d).

According to the line scan analysis presented in Fig. 9, the layer-by-layer structures consisted of copper-rich layers adjacent to iron-rich layers. Based on the comparison of the chemical composition of the copper-rich layer and copper–nickel base metal, this zone belonged to the copper–nickel base metal. However, the iron-rich layer did not match the chemical composition of steel base metal. The highest mass percentages of copper and chromium in the iron-rich layer were 9% and 30%, respectively. The iron-rich layer had a higher copper percentage, which increased to 31wt% in some layers.

The high percentages of nickel and copper as austenite stabilizers could promote the formation of austenite phase. Generally, welding of austenite stainless steel can cause defects, including formation of the brittle phase, hot cracks, and carbide–chrome in grain boundaries. Copper, as an austenite-forming element, eliminates the δ-ferrite and sigma phases. Furthermore, the copper–nickel alloy limits the sigma phase by increasing the cooling rate from 600 to 800°C [22].

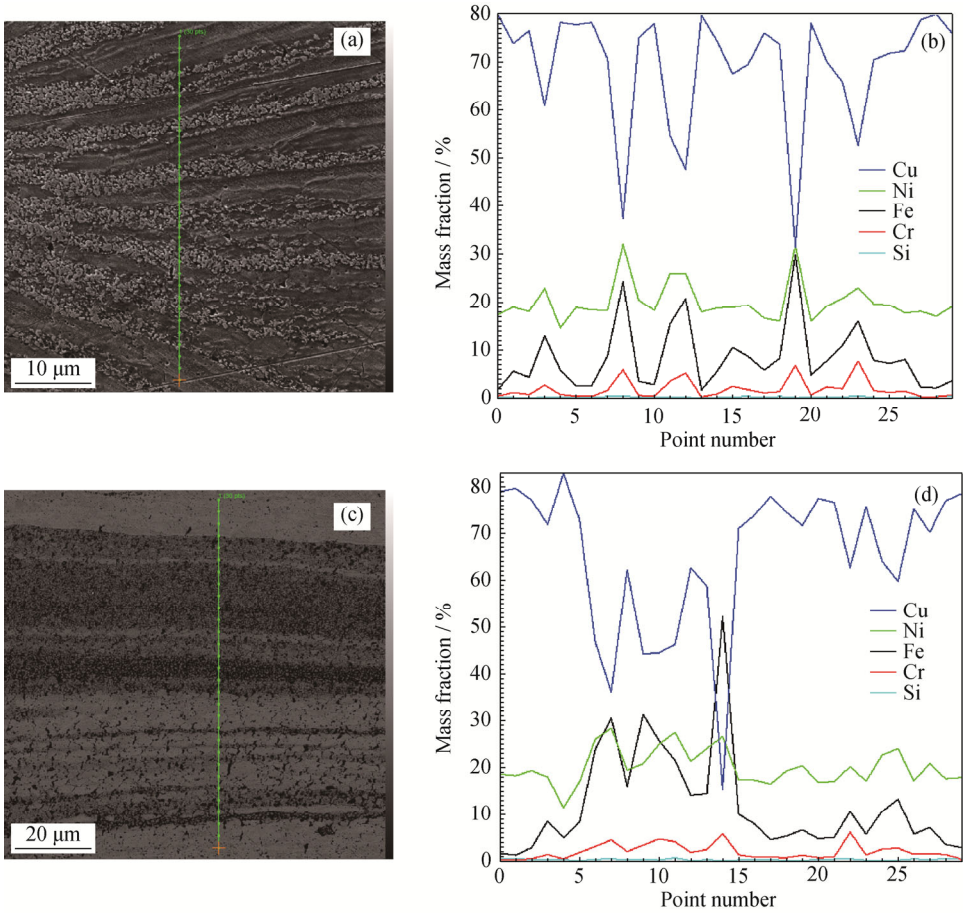


**Fig. 9. SEM image and line scans of chemical elements at the layer structure: (a, b) zone I in Fig. 6(a): (c, d) Fig. 5(f).**

The sigma phase is very hard and brittle. Its value increases by increasing the percentage of chromium, molybdenum, and silicon, but decreases by increasing the nitrogen, nickel, and carbon contents. Prevention of sigma phase formation in stainless steel is difficult when the chrome percentage is about 20wt%. When the chrome percentage is less than 20wt%, the sigma phase is not observable in austenite stainless steels. Due to the very low amount of chrome (up to 9wt%) in the layered structure, formation of sigma phase is not expected.

Fig. 10 shows the XRD analysis of the iron-rich zone in the layered structure (point A in Fig. 6(c)); the austenite phase is the only existing phase in this zone. The high percentage of nickel and copper prevented the formation of sigma phase as expected. The line scan analysis (Fig. 9) indicated that nickel concentrations reduced in layer boundaries but increased in the iron-rich layers due to nickel migration from the interface to iron-rich layers.

According to the EDS results (Fig. 11(a)) regarding point A in Fig. 6(c), the nickel and copper percentages were 24wt% and 21wt%, respectively, indicating the diffusion of

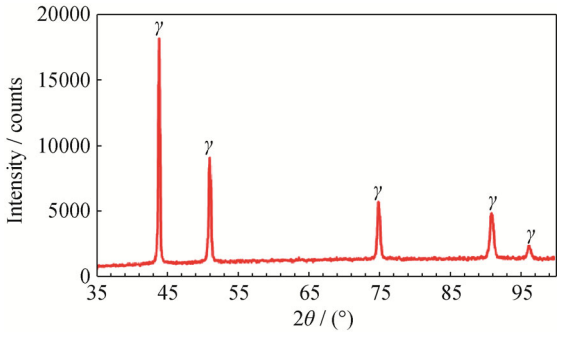


**Fig. 10. XRD pattern of iron rich layer structure.**

nickel and copper from the copper–nickel alloy at the interface of steel alloy due to the close proximity of this region to the tool shoulder and high temperature of the zone. According to the EDS results (Fig. 11(b)), regardless of the increased percentage of copper and nickel in the grain boundaries of the recrystallized zone on the steel side, the high percentage of chrome indicates the increased effect of this element by moving toward the stir zone of the stainless steel. Carbon present in the grain boundaries indicates chrome carbide formation at the joint interface near the tool shoulder.

The chemical compositions of these spots indicate that chrome and carbon move toward high-energy zones and form chrome carbide. Formation of carbide and a chrome-free zone around the grain boundary can severely degrade corrosion resistance of the joint. Analysis of point C (Fig. 11(c)) indicates that this zone belongs to 304 stainless steel. The transient zone in the joint interface can affect the mechanical properties of the joint. Partial diffusion and formation of iron- and copper-rich layers, as shown in Fig. 9, are also observed in zone I of Fig. 5(a).

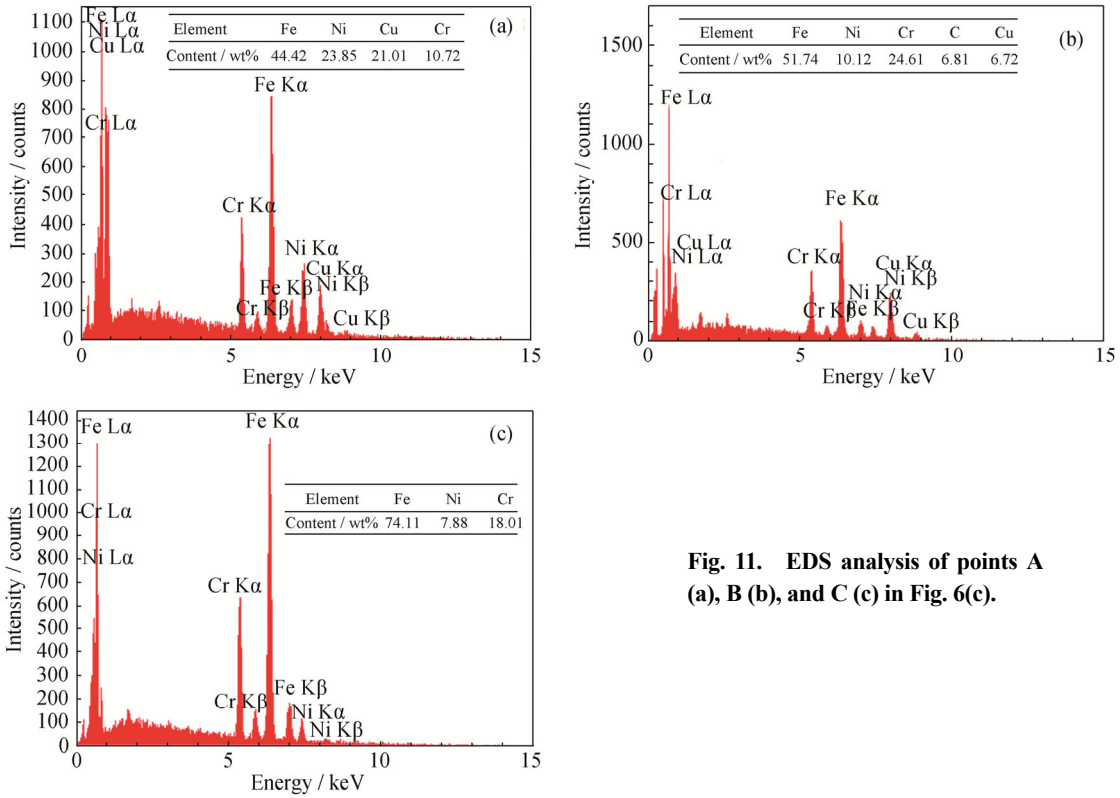


**Fig. 11. EDS analysis of points A (a), B (b), and C (c) in Fig. 6(c).**

### 3.3. Hardness evaluation

The joint microhardness profile at the mid-thickness of the weld cross section is presented in Fig. 12. Hardness of the stir zone increases by moving from the steel base metal. According to the Hall-Petch equation, smaller grains have greater hardness; accordingly, hardness increases by decreasing the grain size and increasing the particle boundary density. Hardness near the interface fluctuates considering the layer-by-layer structure. This structure produces important features, such as non-uniform hardness profiles and stress concentration zones. The stir zone on the copper–nickel side had a more uniform hardness profile and lower quantity. Hardness gradually decreased to the level of copper–nickel base metal by moving toward the copper–nickel base metal.

### 3.4. Tensile properties and fractography

The stress–strain curves for the base metals and joint are shown in Fig. 13. The yield strength and tensile strength of the joint are 103 MPa and 285 MPa, respectively, while elongation is 21%; these values are significantly lower than the corresponding values in the base metals. Tensile strength and elongation of joint were 84% and 65% of the corresponding values, respectively in the copper–nickel base metal. It should be noted that fracture occurred in the weld nugget and at the interface of steel and copper–nickel. The hardness profile shows sudden fluctuations, which cause stress concentrations and joint strength degradation.

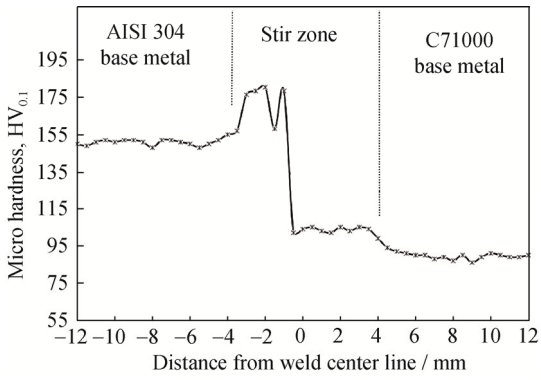


**Fig. 12. Microhardness profiles of cross-section of joint No. 6.**

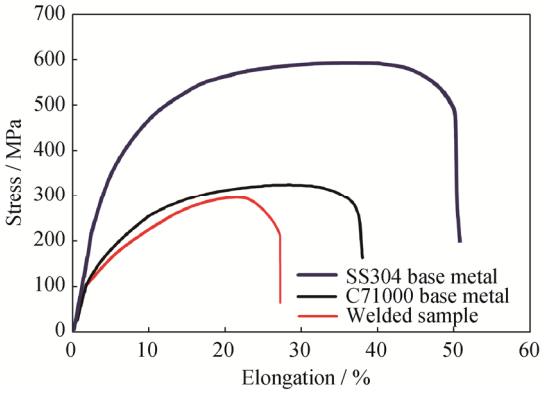


**Fig. 13. Stress–strain curve of base metals and welded sample No. 6.**

The fractured cross section was investigated by SEM after the tensile test. Fig. 14 shows the fractured section and SEM image. The SEM image of the fracture zone shows a brittle cleavage fracture, along with plastic deformation and small uniform holes on the surface. In the brittle cleavage fracture, the crack propagation corresponds to the successive and repeated breaking of atomic bonds along specific crystallographic planes. The fracture surface has a faceted texture because of different orientations of the cleavage planes in the grains. In this type of fracture, no substantial plastic deformation occurs and the crack propagates very fast, nearly perpendicular to the direction of the applied stress. In the ductile fracture mode, spherical dimples correspond to microvoids initiating crack formation. Each dimple is half the size of the microvoid, which is formed and then separated during the fracture process. In the welded sample, brittle and ductile failures simultaneously occurred, which could be attributed to the transient zone (Fig. 12) and sudden fluctuations in the hardness of the sample.

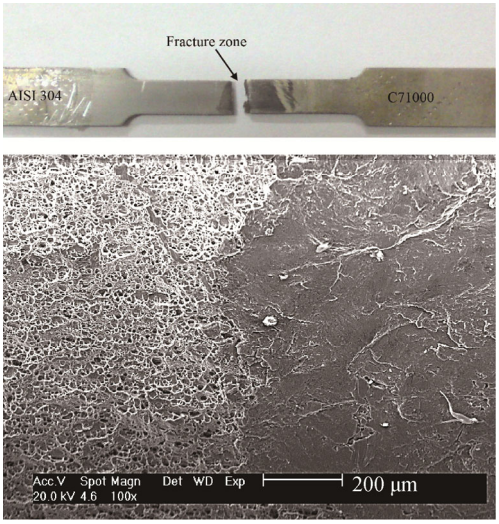


**Fig. 14. SEM image of fracture surface of the joint No. 6.**

## 4. Conclusions

The present study investigated the friction-stir welding of C71000 and AISI304 stainless steel with a cylindrical pin tool and the following results were obtained.

(1) Lack of proper material flow occurred as a result of low temperature at a rotational-to-linear speed ratio of 10 r/mm; therefore, there was not adequate material to fill the hole as the tool traveled forward on the advancing side (stainless steel). In case of rotational-to-linear speed ratio of greater than 20 r/mm, the high heat input produced a higher temperature gradient and resulted in the formation of longitudinal cracks as a result of thermal stress in the joint section.

(2) The grain size on the copper–nickel side was larger than that of the stainless steel side. The stirring phenomena during friction-stir welding eliminated annealing twins in the stainless steel base metal and a uniform microstructure with small equiaxed grains formed in the stir zone. Tensile strength and elongation of joint were 84% and 65% of the corresponding values, respectively in the copper–nickel base metal. The fracture surface indicated brittle cleavage and plastic deformation behaviors.

(3) Heat and plastic deformation caused element diffusion at copper- and iron-rich layers in the stir zone. Nickel and copper, as austenite stabilizers, led to the formation of austenite phase in the iron-rich layers. Chrome and carbon were transferred to grain boundaries, which were high-energy zones, and formed chrome carbide. The layer-by-layer structure and precipitation at the interface made the hardness profile non-uniform and formed possible stress concentration zones.

## Acknowledgement

The author acknowledges the funding support of Babol Noshirvani University of Technology (No. BNUT/370167/97).

## References

[1] M. Metikoš-Huković, R. Babić, I. Škugor, and Z. Grubač, Copper-nickel alloys modified with thin surface films: Corrosion behaviour in the presence of chloride ions, *Corros. Sci.*, 53(2011), No. 1, p. 347.

[2] M. Metikoš-Huković, R. Babić, I. Škugor Rončević, and Z. Grubač, Corrosion resistance of copper–nickel alloy under fluid jet impingement, *Desalination*, 276(2011), No. 1-3, p. 228.

[3] P. Carol, Corrosion and biofouling resistance evaluation of 90-10 copper–nickel, *Copper Development Association*,

2005, No. 63, p. 8.

[4] S.G. Shiri, M. Nazarzadeh, M. Shariftabar, and M.S. Afarani, Gas tungsten arc welding of CP-copper to 304 stainless steel using different filler materials, *Trans. Nonferrous Met. Soc. China*, 22(2012), No. 12, p. 2937.

[5] C.W. Yao, B.S. Xu, X.C. Zhang, J. Huang, J. Fu, and Y.X. Wu, Interface microstructure and mechanical properties of laser welding copper-steel dissimilar joint, *Opt. Lasers Eng.*, 47(2009), No. 7-8, p. 807.

[6] I. Magnabosco, P. Ferro, F. Bonollo, and L. Arnberg, An investigation of fusion zone microstructures in electron beam welding of copper-stainless steel, *Mater. Sci. Eng. A*, 424(2006), No. 1-2, p. 163.

[7] T.A. May and A.C. Spowage, Characterisation of dissimilar joints in laser welding of steel–kovar, copper–steel and copper–aluminium, *Mater. Sci. Eng. A*, 374(2004), No. 1-2, p. 224.

[8] C. Roy, V.V. Pavanan, G. Vishnu, and P.R. Hari, M. Arivarasu, M. Manikandan, D. Ramkumar, and N. Arivazhagan, Characterization of metallurgical and mechanical properties of commercially pure copper and AISI 304 dissimilar weldments, *Procedia Mater. Sci.*, 5(2014), p. 2503.

[9] M. Velu and S. Bhat, Metallurgical and mechanical examinations of steel–copper joints arc welded using bronze and nickel-base superalloy filler materials, *Mater. Des.*, 47(2013), p. 793.

[10] Y. Imani, M.K. Besharati, and M. Guillot, Improving friction stir welding between copper and 304L stainless steel, *Adv. Mater. Res.*, 409(2012), p. 263.

[11] A.J. Ramirez, D.M. Benati, and H.C. Fals, Effect of tool offset on dissimilar Cu–AISI 316 stainless steel friction stir welding, [in] *Proceeding of the Twenty-first International Offshore and Polar Engineering Conference*, Maui, Hawaii, USA, 2011, p. 548.

[12] A. Najafkhani, K. Zangeneh-Madar, and H. Abbaszadeh, Evaluation of microstructure and mechanical properties of friction stir welded copper/316L stainless steel dissimilar metals, *Int. J. ISSI*, 7(2010), No. 2, p. 21.

[13] M. Shamsujjoha, B.K. Jasthi, M. West, and C. Widener, Microstructure and mechanical properties of FSW lap joint between pure copper and 1018 mild steel using refractory metal pin tools, [in] *Friction Stir Welding and Processing VII*, TMS, San Antonio, Texas, 2013, p. 151.

[14] M. Jafari, M. Abbasi, D. Poursina, A. Gheysarian, and B. Bagheri, Microstructures and mechanical properties of friction stir welded dissimilar steel–copper joints, *J. Mech. Sci. Technol.*, 31(2017), No. 3, p. 1135.

[15] Copper Development Association Inc., *Copper–Nickel Welding and Fabrication*, Copper Development Association Inc., McLean, Virginia [2013-02-01]. http://www.copper.org/applications/marine/cuni/fabrication/welding_and_fabrication.html

[16] Smiths Metal Centres, *304/304L Stainless Steel Data Sheet*, Smiths Metal Centres, Clerkenwell, London [2007-03-05]. http://www.smithmetal.com/datasheets.htm.

[17] S.H.C. Park, Y.S. Sato, H. Kokawa, K. Okamoto, S. Hirano, and M. Inagaki, Rapid formation of the sigma phase in 304 stainless steel during friction stir welding, *Scripta Mater.*, 49(2003), No. 12, p. 1175.

[18] Y.V.R.K. Prasad, K.P. Rao, and S. Sasidhara, *Hot Working Guide: A Compendium of Processing Maps*, ASM International, Materials Park, Ohio, 2015, p. 168.

[19] Y. Sun and H. Fujii, Effect of abnormal grain growth on microstructure and mechanical properties of friction stir welded SPCC steel plates, *Mater. Sci. Eng. A*, 694(2017), p. 81.

[20] H. Jamshidi Aval, Influences of pin profile on the mechanical and microstructural behaviors in dissimilar friction stir welded AA6082–AA7075 butt joint, *Mater. Des.*, 67(2015), p. 413.

[21] N. Kumar, R.S. Mishra, and W. Yuan, *Friction Stir Welding of Dissimilar Alloys and Materials*, Butterworth-Heinemann, Oxford, 2015, p. 16.

[22] J.C. Lippold, *Welding Metallurgy and Weldability*, John Wiley & Sons, Hoboken, New Jersey, 2014, p. 9.